Journal of The Electrochemical Society

OPEN ACCESS

Bulk and Surface Stabilization Process of Metastable Li-Rich Disordered Rocksalt Oxyfluorides as Efficient Cathode Materials

To cite this article: Y. Shirazi Moghadam *et al* 2022 *J. Electrochem. Soc.* **169** 120514

Journal of The Electrochemical Society, 2022 **169** 120514

Bulk and Surface Stabilization Process of Metastable Li-Rich Disordered Rocksalt Oxyfluorides as Efficient Cathode Materials

Y. Shirazi Moghadam,[1] A. El Kharbachi,[1,z] G. Melinte,[1,2] T. Diemant,[1] and M. Fichtner[1,2]

[1]*Helmholtz Institute Ulm (HIU), Helmholtzstr. 11, 89081 Ulm, Germany*
[2]*Institute of Nanotechnology, Karlsruhe Institute of Technology (KIT), P.O. Box 3640, 76021 Karlsruhe, Germany*

Manganese based disordered rocksalt systems have attracted attention as Co-free and high capacity cathode materials for Li-ion batteries. However, for a practical application these materials are considered as metastable and exhibit too limited cyclability. In order to improve the structural stability of the disordered rocksalt $Li_{1+x}Mn_{2/3}Ti_{1/3}O_2F_x$ ($0 \leqslant x \leqslant 1$) system during cycling, we have introduced a mild temperature heat treatment process under reducing atmosphere, which is intended to overcome the structural anomalies formed during the mechanochemical synthesis. The heat-treated samples presented better electrochemical properties, which are ascribed to a structural defect mitigation process both at the surface and in the bulk, resulting in improved crystal structure stability. In addition, the optimized particle size and the smaller BET surface area induced by the recrystallization contributes to the observed enhanced performance. Among the studied compositions, the heat treated $Li_2Mn_{2/3}Ti_{1/3}O_2F$ sample displayed better electrochemical performance with a discharge capacity of 165 mAh g^{-1} after 100 cycles at 0.1 C (~80% of the initial capacity), when combined with further conditioning of the cells. The results point explicitly towards a guided stabilization approach, which could have a beneficial effect regarding the application of DRS oxyfluoride materials for sustainable LIBs.
 [DOI: 10.1149/1945-7111/acaa62]

Manuscript submitted August 19, 2022; revised manuscript received November 29, 2022. Published December 19, 2022.

Supplementary material for this article is available online

Today's high demand for Li-ion batteries (LIBs) affirms the need to replace critical metals such as cobalt and nickel with alternative transition metals (TMs). Unlike many candidate cathode materials, novel disordered rocksalt (DRS) oxyfluorides can be synthesized with a multitude of TMs and their combinations.[1–4] A typical DRS material with a cubic close packed structure allows the creation of percolation pathways within the material to support Li ions diffusion, which is necessary for (de)charging the battery.[5] Moreover, the cation disorder contributes to the enhancement of the structural and thermodynamic stability of Li-rich cathode materials with better kinetics.[6] Besides, several lithium excess phases based on vanadium and manganese with high capacities have been introduced.[2,4, 7–11] However, vanadium is toxic and expensive, which may be a hindrance for large scale production.[1,4] Moreover, the synthesized materials turned out to be metastable. As alternative, cathode materials based on manganese have the potential to attract attention due to their good structural stability and environmental friendliness.[12] Partial substitution of oxygen with fluorine is one of the strategies to allow large oxidation state changes of the cations, while the latter can stabilize the structure and enhance the electrochemical properties.[13–15]

Despite the advantages of oxyfluoride materials in terms of offering high redox capacity and stability, all presented systems and compositions up to now still suffer from short life span and degradation already after few cycles. Recently, we reported the first $Li_2Mn_{2/3}Ti_{1/3}O_2F$ optimized structure by Ti-substitution to achieve high yield Mn^{4+}/Mn^{2+} double-redox reaction without any additional treatment or additives.[16,17] For long-term cyclability under voltage variation and surrounded electrolyte, it appeared to be essential to stabilize the synthesized materials further after observation of their initial electrochemical properties. The DRS materials resulting from ball-milling synthesis exhibit a metastability, likely favored by the presence of microstrain and significant surface defect domains in the order of the size of the bulk particles.

To overcome these structural anomalies, performing heat treatment can be an efficient way to increase the homogeneity between surface and bulk for battery grade materials. However, sintering of air-sensitive oxyfluoride materials has been a challenge since the discovery of this class of materials in 2015, due to the low temperature stability of these materials. Such experimental protocols are not straightforward and require a careful design.[6,18] Up to now, several works on heat treatment process have been reported for disordered rocksalt oxides such as $Li_{1.25}Nb_{0.25}V_{0.5}O_2$, $Li_{1.3}Mn_{0.4}Nb_{0.3}O_2$, $Li_{1.3}Fe_{0.4}Nb_{0.3}O_2$, $Li_{1.233}Mo_{0.467}Cr_{0.3}O_2$ and Li_2VTiO_4,[19–22] as well as for vanadium and nickel-based oxyfluoride compounds; however, the treatments resulted in changes of the crystal structure and phase segregation.[23,24] In spite of the growing interest in DRS oxyfluorides as cathode materials, studies on stabilization processes of these class of compounds are still limited.

Herein, we report our recent findings enabling the implementation of a successful procedure for stabilization of oxyfluoride materials with a DRS structure by a mild temperature sintering process under reducing atmosphere. Different microstructural features have been elucidated for different model samples with varied composition $Li_{1+x}Mn_{2/3}Ti_{1/3}O_2F_x$ ($0 \leqslant x \leqslant 1$). The main focus of this work is then to provide an input on the (meta-) stability of DRS oxyfluoride materials, mainly during high-voltage cycling conditions. Furthermore, other interface factors such as calendar aging and conditioning of the cells before cycling are also studied, as a complement to the heat-treatment process, with the aim to find a compromise between the delivered energy density and stability of the disordered rocksalt cathode materials under different Li-ion half-cell operation conditions.

Experimental

The following precursor materials were purchased from Alfa Aesar with the highest purity: Li_2O (99.7%), Mn_2O_3 (99%), Ti_2O_3 (99.8%) and LiF (99.9%). In brief, $Li_{1+x}Mn_{2/3}Ti_{1/3}O_2F_x$ ($0 \leqslant x \leqslant 1$) (LMTOF) product powders of significant nano-crystallinity were experimentally obtained by high-energy ball milling starting from the stoichiometric ratios of the precursors; more details of this part of the synthesis procedure are reported elsewhere.[16] According to the F/anion ratio, the synthesized samples are referred as LMO ($LiMn_{2/3}Ti_{1/3}O_2$), LMOF11 ($Li_{1.25}Mn_{2/3}Ti_{1/3}O_2F_{0.25}$), LMOF20 ($Li_{1.5}Mn_{2/3}Ti_{1/3}O_2F_{0.5}$) and LMOF33 ($Li_2Mn_{2/3}Ti_{1/3}O_2F$).

[z]E-mail: kharbachi@kit.edu

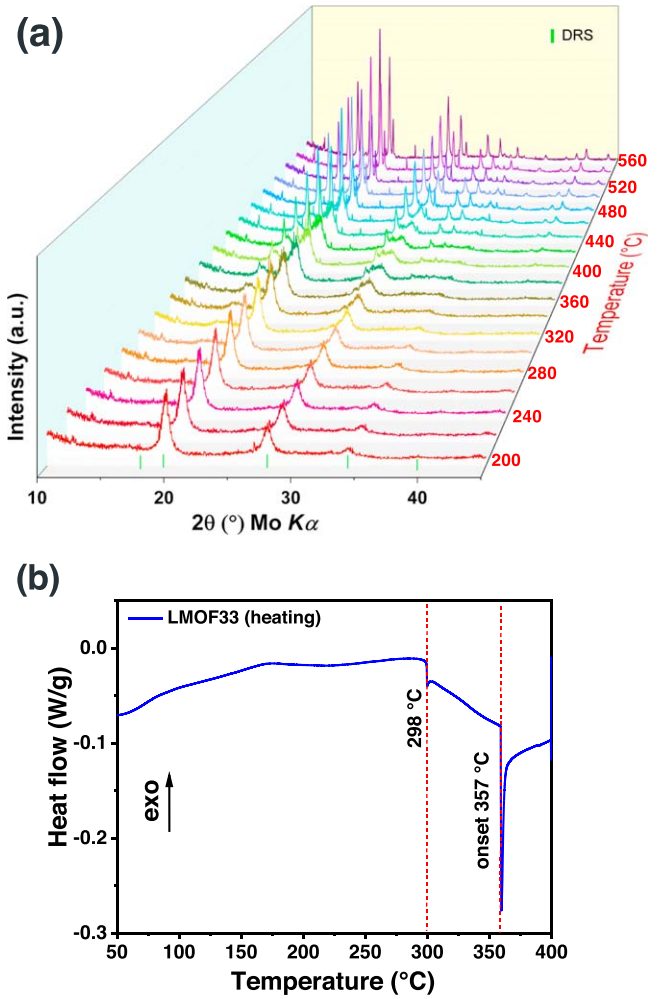

Figure 1. (a) In-situ HT-XRD patterns of the LMOF33 sample measured from 200 to 560 °C and (b) its thermal behavior from 40 to 400 °C measured by DSC with a heating rate of 10 °C min^{-1}.

In the next step, 500 mg active material was cold-pressed up to 240 MPa using a 10 mm die-set. The resulting pellets were put in stainless steel-cells covered with a lid of the same material. The cells were then placed in an alumina crucible boat, which was transferred into a 43 cm long quartz tube under argon atmosphere. The tube was then put in a tubular oven under forming gas flow (~50 ml min^{-1}), heated with a rate of 1.5 °C min^{-1} up to 280 °C, kept there for 5 h and finally self-cooled down to room temperature (RT). This procedure was repeated two more times, resulting in a total heating time of 15 h. After heat treatment the pellets were ground to fine particles.

Crystalline phase detection was accomplished using a STOE STADI-P X-ray diffractometer with Mo K_α radiation (λ = 0.70932 Å), in transmission geometry in a 2θ range of 10–60 degrees and step size of 0.02°. The diffractometer is equipped with a high temperature (HT) furnace accessory, which can be employed for HT-PXRD (high temperature powder X-ray diffraction) measurements to study the phase evolution of the LMTOF system. To do so, the sample temperature was raised at 5 °C min^{-1} and an XRD measurement was taken while keeping the temperature constant for one hour. Consequently, a series of XRD patterns were taken every 20 °C. Rietveld refinement was performed using FullProf Suite software. For Rietveld refinement of the XRD patterns, we used the *Fm*-3*m* space group as the main phase, with a disordered rocksalt structure. The cations are occupying 4a/(0 0 0) Wyckoff/(x y z) positions and the anions occupying 4b/(1/2 1/2 1/2) positions. The main microstructural parameters that we fitted were: lattice parameter, occupancy and the thermal factor B. Also, we used Pseudo-Voigt peak shape model for fitting the peaks.

The thermal stability of the as synthesized $Li_2Mn_{2/3}Ti_{1/3}O_2F$ powder was determined using a differential scanning calorimeter (DSC) from TA Instruments (Discovery DSC CFN-50). Around 10 mg of the powder sample was crimp-sealed in an Al pan in an Ar filled glovebox. The measurements were performed from 40 to 400 °C under nitrogen atmosphere with a heating rate of 10 °C min^{-1}. The morphology of the particles was analyzed by scanning electron microscopy (SEM with a ZEISS GEMINI Cross beam 350 Field Emission SEM, using a transfer box from the glovebox to the SEM vacuum chamber. The particle size of the samples was calculated using Image J software based on SEM images. For this calculation, 200 particles were selected and their diameters were obtained, and then the average particle size for each sample was calculated.

For transmission electron microscopy (TEM) measurements the samples were prepared inside a glovebox and transferred to the microscope without air exposure using a vacuum transfer holder. The dry powder was directly dispersed on the TEM holey carbon membrane without the use of solvents. The measurements were performed using a Themis300 electron microscope working at 300 kV and equipped with a DCOR probe corrector and a Super X EDX detector. The *K*-lines of O, F, Ti and Mn were used for quantification in STEM-EDX elemental mapping. The Brunauer–Emmet–Teller (BET) specific surface area was determined from N_2 adsorption using a QuantaChrome-ASIQA 0010–5 analyzer at liquid nitrogen temperature.

The oxidation state of Ti and Mn atoms in the topmost surface layer (sampling depth ~3–5 nm) of a pristine LMOF33 powder sample was investigated by X-ray photoelectron spectroscopy (XPS) measurements (Specs XPS system with XR50-M X-ray source and Phoibos 150 energy analyzer) using monochromatized Al K_α radiation (400 W, 15 kV), a detection angle of 45°, and analyzer pass energies of 90 eV and 30 eV for survey and detail spectra, respectively. For binding energy calibration, the C 1s peak of adventitious carbon was set to 284.8 eV. Peak fitting was done with CasaXPS software using Shirley-type backgrounds and Gaussian-Lorentzian peak profiles.

The cyclic voltammograms (CV) were measured by using an electrochemical station VMP-3 potentiostat from Bio-Logic® at a scan rate 0.5 mV s^{-1} with the voltage ranging from 1.5 to 4.0 V. Electrochemical impedance spectra (EIS) were measured using a VMP-3 impedance analyzer in the frequency range from 100 kHz to 10 mHz. For the EIS measurements of the aged samples before/after cycling (up to 10 cycles), half cells were used. And for the aged samples after the 1st and 100th cycle (prolonged cycling) symmetric cathode-cathode cells with similar mass loading were employed to decouple counter electrode contribution, hence, the increase in impedance can be solely attributed to the cathode material.

To prepare a cathode film from the $Li_{1+x}Mn_{2/3}Ti_{1/3}O_2F_x$, ($0 \leqslant x \leqslant 1$) powders, the active compounds and carbon black (Timcal, Super C65) were mixed together for three hours in an Ar-filled 20 ml silicon nitride vial containing 10 balls (Ø 2 mm) of the same material. The grinding was carried out at low rate of 200 rpm, using a Fritsch P7 premium line planetary ball mill. The composite was then sieved using 200 mesh sieve. For the slurry, first the polyvinylidene fluoride (PVDF) as a binder was mixed with *N*-methyl-2-pyrrolidone (NMP) as solvent for 5 min. Then the mixture of active material and carbon black was added in two steps, each of 5 min mixing. For the slurry making process, we used 4 cm capsules with 5 small balls (4 mm) as grinding agent compatible with a Thinky mixer (ARE-250, Thinky Inc.). The slurry was then coated on an aluminum foil with an automatic doctor blade in an argon filled glovebox. The composite coating was dried at 120 °C overnight in vacuum oven. Each working electrode contained ~0.9 mg cm^{2-} of active material. For all cycling tests, Swagelok cells were fabricated in an argon filled glovebox. As electrolyte, 140 μl of $LiPF_6$ (1 M) in ethylene carbonate and ethyl methyl carbonate (EC/DEC) solution (1:1, BASF®) was used. Lithium foils and Whatman® glass fiber were used, respectively, as counter/reference electrode and separator. The assembled Swagelok cells were tested at 25 °C in

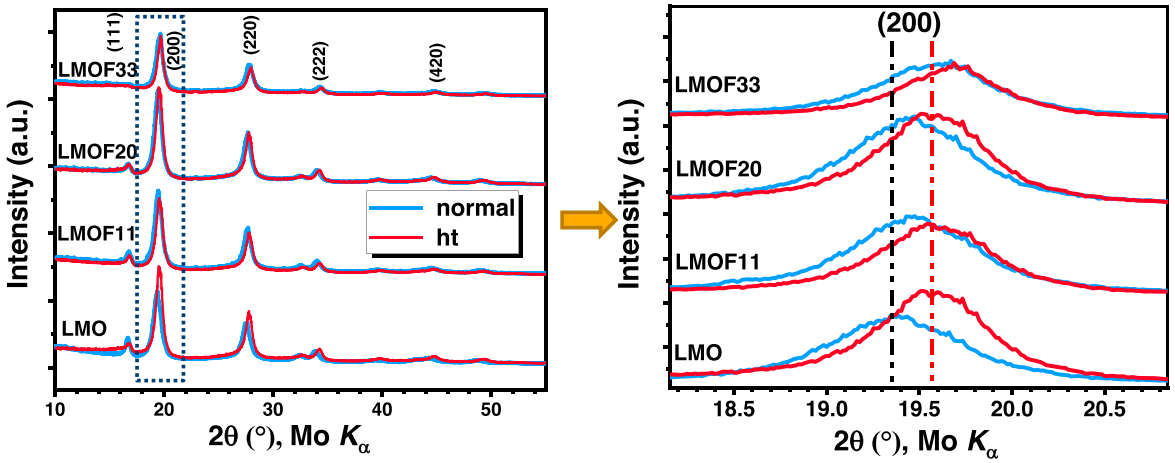

Figure 2. Comparison of the XRD patterns of the synthesized compounds before and after heat treatment. Inset: Zoom in the (200) reflection.

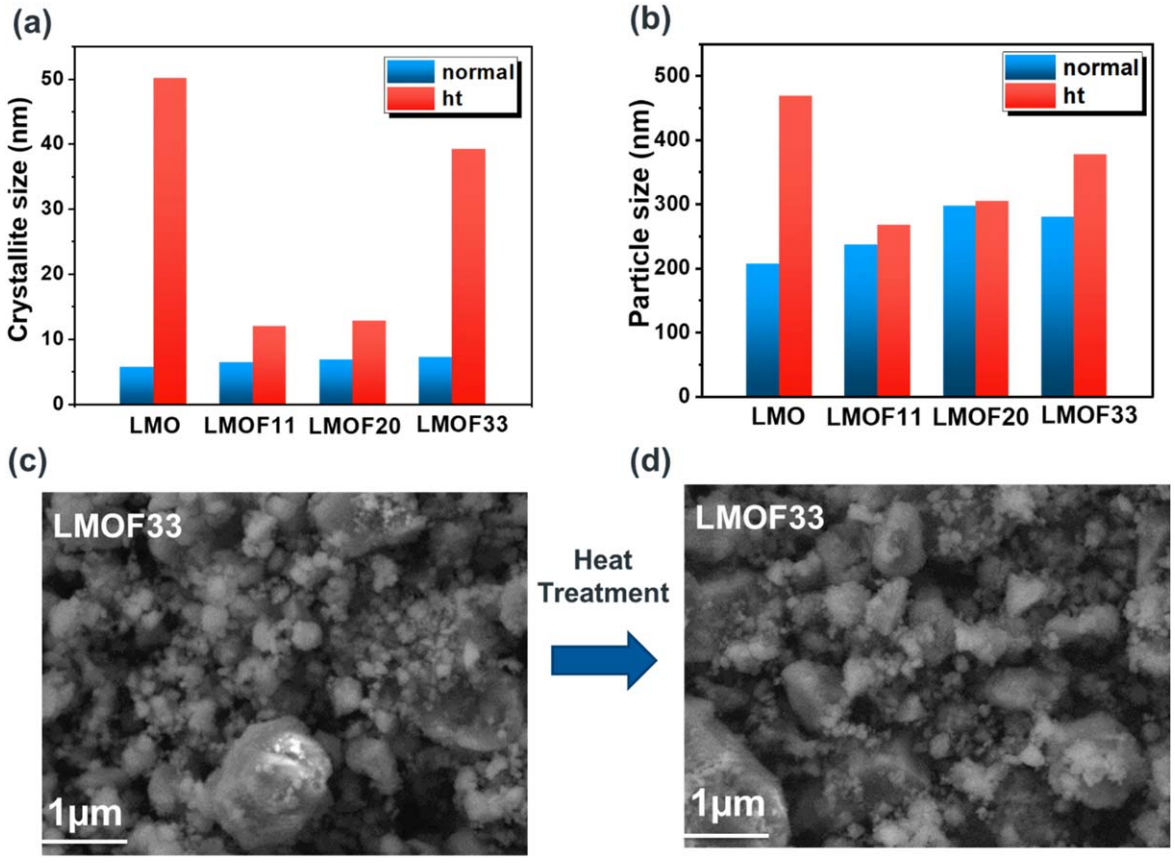

Figure 3. Comparison of the (a) crystallite size and (b) particle size of the samples before (left bar) and after heat treatment (right bar). SEM images of the LMOF33 sample (c) before and (d) after heat treatment.

climate chambers using an Arbin BT2000 electrochemical workstation. The specific capacity of the cells was calculated based on the amount of active material (60 wt%) in the cathode film. For calendar aging of the electrodes, Swagelok-type cells were assembled in an argon filled glovebox and aged as-assembled before cycling for different time periods from 1 day to 4 weeks.

Results and Discussion

Structural and chemical characterization of the pristine materials.—*The p*hase stability of LMOF33 ($Li_2Mn_{2/3}Ti_{1/3}O_2F$) was investigated using high temperature X-ray diffraction (HT-XRD) from 200 to 560 °C. Figure 1a indicates that the structure remains at 200 °C the same as at RT, being identified as disordered rocksalt structure. In contrast, the XRD pattern at 300 °C shows the first deformation of the peaks, and after further increasing the temperature the DRS phase starts to vanish at 360 °C (see 2D plot Fig. S1). At 500 °C, the transformation of the phase can be seen. Upon further heating to 560 °C no additional phases were observed. The phase analysis of the sample heated up to 560 °C and cooled back down to RT (Fig. S2a) shows that the phase at 560 °C is consisting of DRS phase together with formation of MnO and LiF. After cooling to RT, it appeared that this phase transformation is only partially reversible, which confirms the limited stability of oxyfluorides with DRS

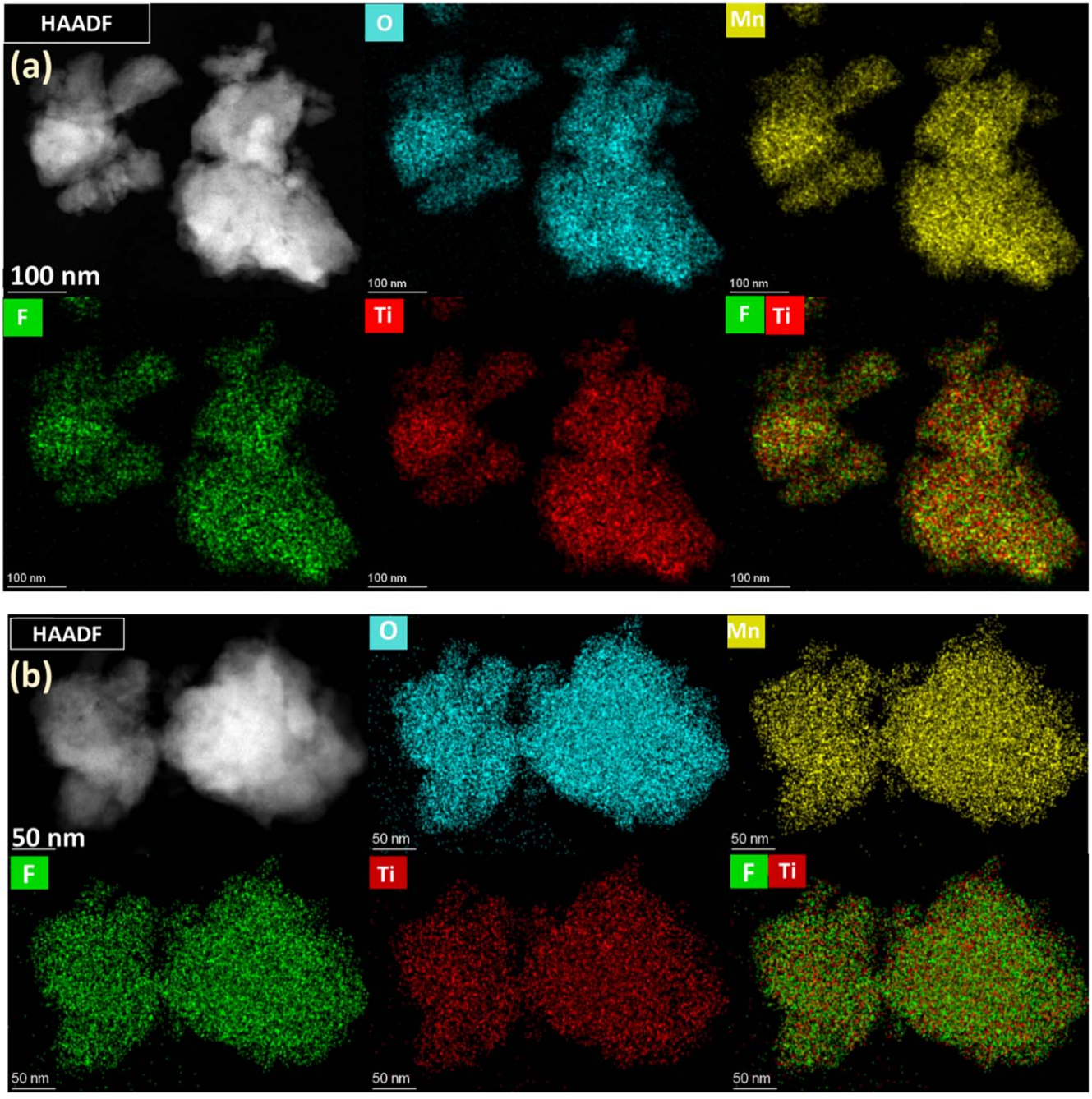

Figure 4. HAADF-TEM images and EDX elemental mapping of the LMOF33 sample (a) before and (b) after heat treatment. The dry powders were analyzed without use of any dispersing solvent.

structure and their sensitivity to high temperatures. Thus, performing a heat treatment process of oxyfluorides for further stabilization is not straight forward, when compared to DRS oxides. In order to support the in situ HT-XRD results, we studied the thermal stability of the sample using DSC from 40 °C–400 °C as shown in Fig. 1b. There were mainly two endothermic peaks, the first (small one) starting at 298 °C, and the second one at 357 °C, as the main phase transition seen in the in situ HT-XRD (Fig. S2).

For a better understanding, the powder after DSC measurement was taken for XRD analysis (Fig. S1b). The results reveal that the phase transition was quasi-reversible and the DRS phase is preserved after cooling to room temperature. However, the intensity of the peak from the (111) plane has increased, which could be due to lithium leaching out of the structure as LiF,[16] in agreement with the observed small peak around $2\theta = 17°$. Based on these results, we have designed the heat treatment process with 280 °C as upper temperature limit, in order to maintain the stability of the DRS structure.

XRD measurements recorded before and after heat treatment for all LMOF compounds show the presence of the disordered rock salt phase, with no obvious additional features from impurities. However, after heat treatment all the patterns showed sharper peaks, with slight shift to higher angles in comparison with non-treated powders (Fig. 2). This corresponds to lattice shrinking of the DRS structure owing to the increase of symmetry. The lattice parameters were found to be 4.208, 4.206 and 4.179 Å before heat treatment, and 4.180, 4.182 and 4.151 Å after heat treatment, respectively, for the LMOF11, LMOF20 and LMOF33 samples. The XRD patterns of the heat-treated samples and the corresponding refinement data parameters are available in the supplementary information (SI) as Fig. S3 and Table SI.

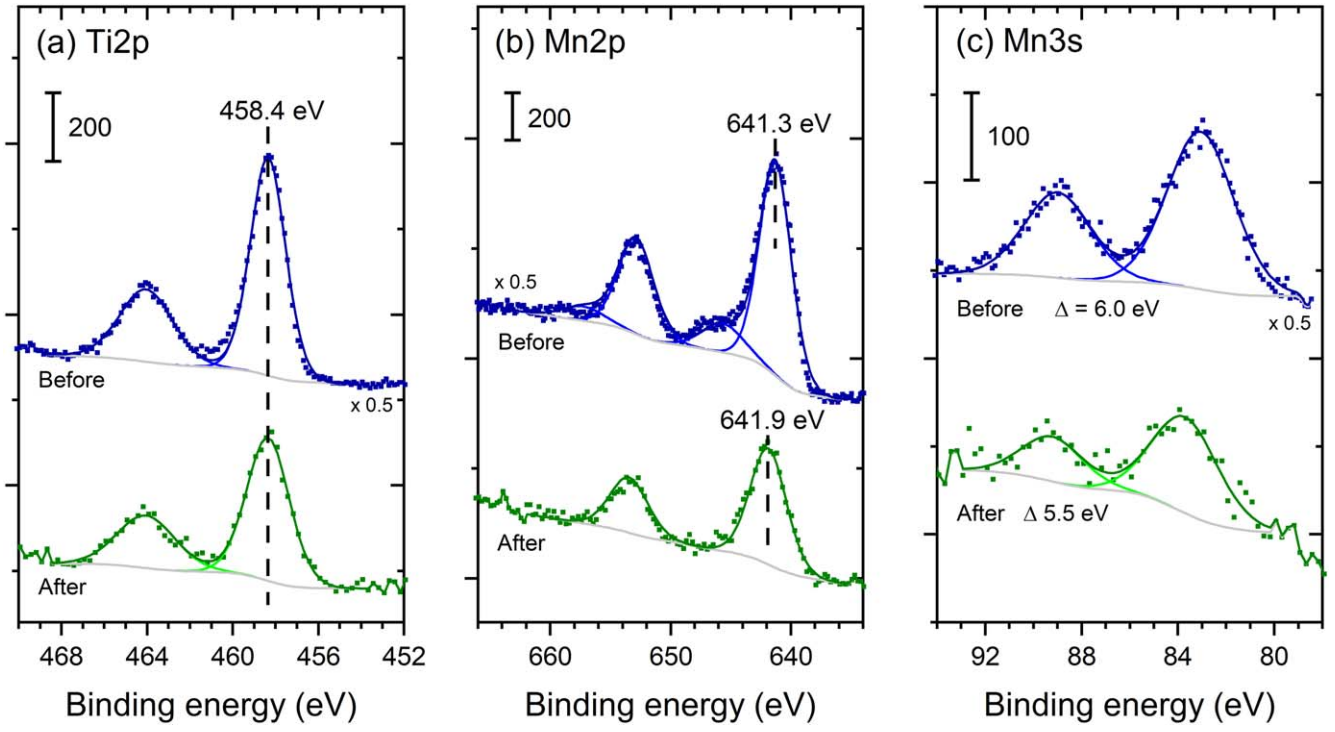

Figure 5. XPS detail spectra in the (a) Ti 2p, (b) Mn 2p, and (c) Mn 3s regions from LMOF33 samples before and after sintering.

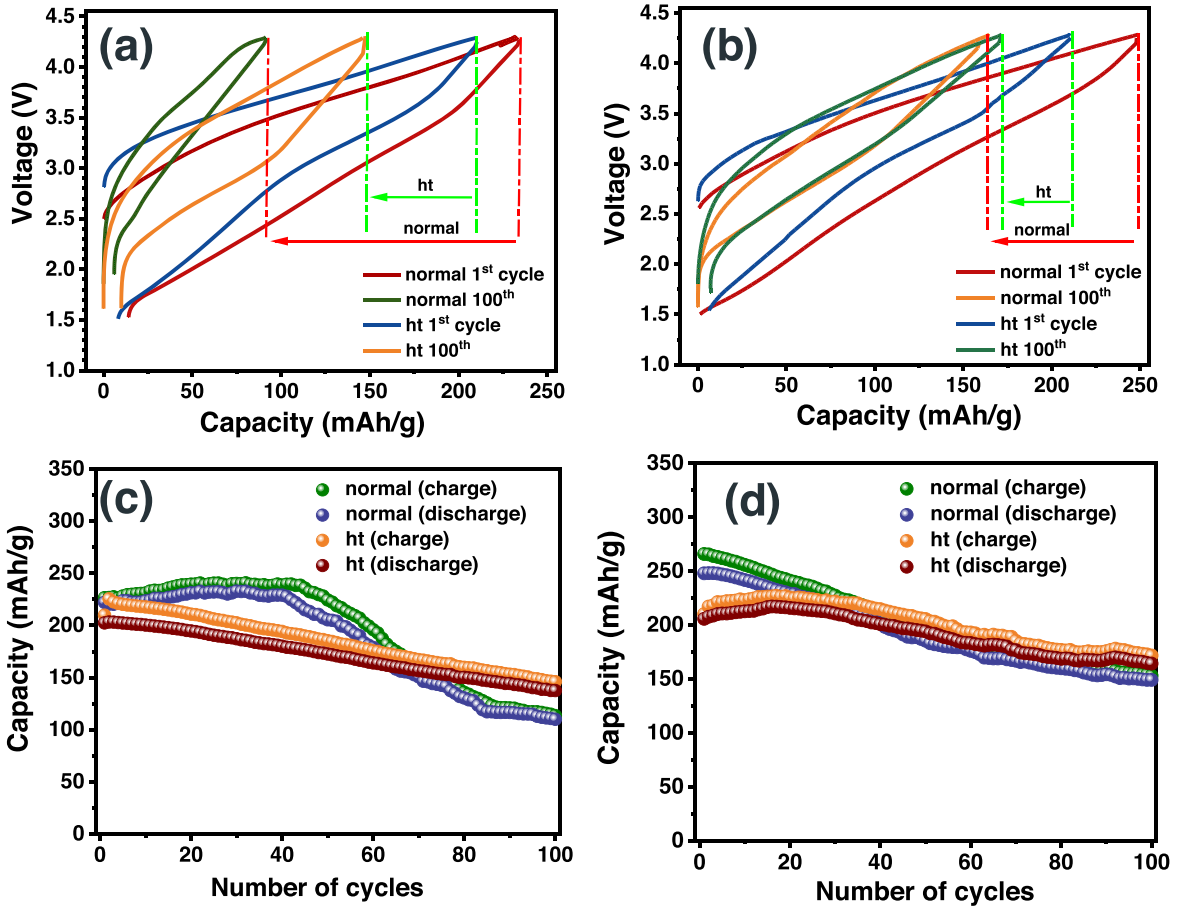

Figure 6. Galvanostatic charge and discharge profiles of the (a) LMOF11 and (b) LMOF33 samples before (normal) and after heat treatment (ht) at the rate of 0.1 C and within the voltage window 1.5–4.3 V; (c)-(d) the corresponding cyclability profiles up to 100 cycles of the same samples, respectively.

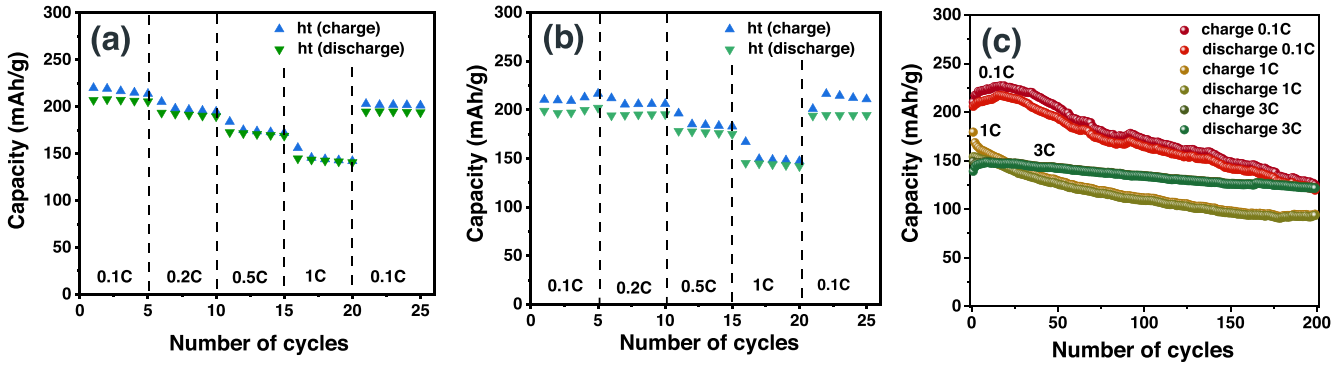

Figure 7. Rate capability plots of the (a) LMOF11 and (b) LMOF33 samples after heat treatment and cycled within the voltage window 1.5–4.3 V. (c) Long-term cycling stability of the LMOF33 sample at different rates and within the voltage window 1.5–4 V.

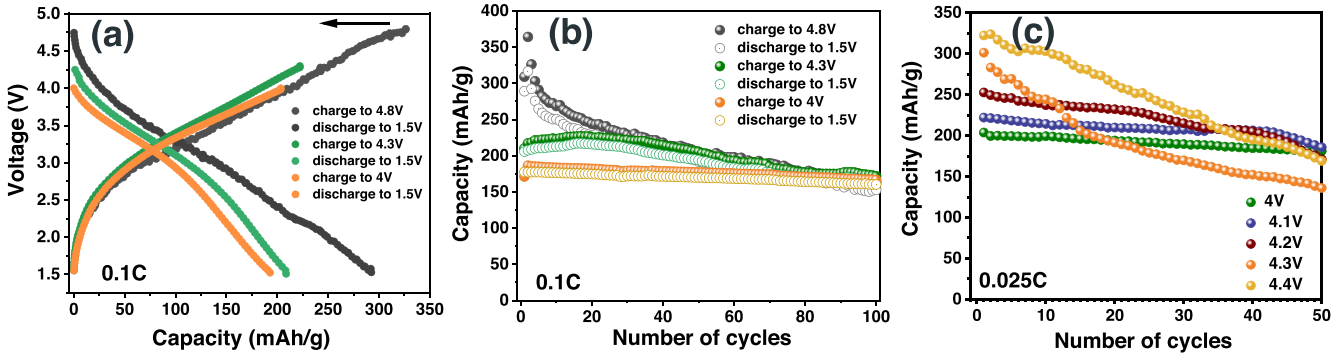

Figure 8. Electrochemical tests of the heat treated LMOF33 sample at different cut-off voltages. (a) Galvanostatic charge and discharge profile at the rate of 0.1 C, (b) related charge-discharge cyclability and (c) capacity retention at the rate of 0.025 C.

The microstructural details before and after treatment are depicted in Fig. 3. As mentioned above, all four compositions have a smaller lattice parameter and bigger crystallite size after heat treatment (according to Williamson-Hall method). The BET measurement for LMOF33 sample revealed that the heat treatment resulted in reduced specific surface area from 5 to 4.5 $m^2\ g^{-1}$ (Fig. S4). This reduction should lead to a better stability of the heat-treated sample in electrochemical cycling, since it will diminish possible side reactions of the active material with the electrolyte at the surface. However, at the same time, the capacity of the heat-treated sample could be smaller due to the increase of the diffusion pathways and low electronic conductivity. The changes in morphology of the LMOF33 sample and increase of average particle size after heat treatment are exemplarily shown in the SEM images of Figs. 3c, 3d. The particle size is an average dimension of solid particles, visible in the SEM images. However, due to the fact that the samples were synthesized by ball milling, there are always some agglomerations present which means the calculated values are a rough estimation for comparison of different samples. Additionally, the following average particle size values 348 and 395 nm were inferred from BET data, before and after heat treatment, respectively. These values, though considering spherical particles and neglecting porosity, are in a good agreement with the calculated values from SEM images, mainly for the sintered powder (380 nm).

The HAADF TEM micrographs of the LMOF33 sample before and after heat treatment are shown in Fig. 4. The EDX elemental mapping clearly demonstrates that the fluorine is well incorporated in the nanostructure, and all the elements are homogenously distributed in the sample before and after heat treatment. Furthermore, the EELS elemental spectra of the LMOF33 sample showed no evident change in the oxidation state of the Ti and Mn cations in different parts of the mapped region (Fig. S5).

In the next step, the chemical state (oxidation state) of Ti and Mn and possible changes induced by the heat treatment were investigated in more detail by XPS measurements. Figure 5 compares exemplarily the results of LMOF33 powder samples before and after heat treatment. First of all, a significant reduction of the peak intensities of all features related to Ti and Mn has to be observed when comparing the results (note the scaling factor in Fig. 5). This can be due to sampling effect of powders with different particle size, but also owing to a significant increase of the C concentration, most probably from pick-up of adventitious carbon species during the heating steps which cover the LMOF33 particle surfaces. This, in turn, reduces the Ti and Mn concentration in the surface layer of the annealed sample. A similar intensity reduction is also observed for all other peaks related to LMOF33 in the Li 1s, O 1s and F 1s regions. The spectra in the Ti 2p region (Fig. 5a) show for both samples a single peak doublet (Ti $2p_{3/2}$ peak at 458.4 eV), which can be attributed to fully oxidized Ti^{4+},[25] indicating that Ti stays fully oxidized also after heat treatment. In contrast, a change of the Mn oxidation state upon heat treatment is clearly visible in the detail spectra in the Mn 2p and Mn 3s regions. In the Mn2p region (Fig. 5b), a main peak doublet is observed (Mn $2p_{3/2}$ peak at 641.3 eV) together with a satellite peak at slightly higher binding energy (~646 eV) before heat treatment. In contrast, the spectrum of the annealed sample shows only the main peak doublet, which is in addition shifted to slightly higher binding energy (Mn $2p_{3/2}$ peak at 641.9 eV). The shift (and the disappearance of the satellite) points to Mn oxidation upon heat treatment, which is also corroborated by the spectra in the Mn 3s region (Fig. 5c). It is well-known that the degree of the multiplet splitting of this peak can be a diagnostic for the Mn oxidation state. For oxides with different Mn oxidation states (from MnO to MnO_2), a splitting of ~6 eV was found for Mn^{2+}, decreasing to ~5.5 eV for Mn^{3+} and ~4.8 eV for Mn^{4+}.[26, 27] While the peak splitting is 6.0 eV before heat treatment, indicating a predominant Mn oxidation state of +II, it decreases to 5.5 eV after heat treatment, hence the Mn oxidation state increases toward +III. This can be related to the fact that during the heat treatment process

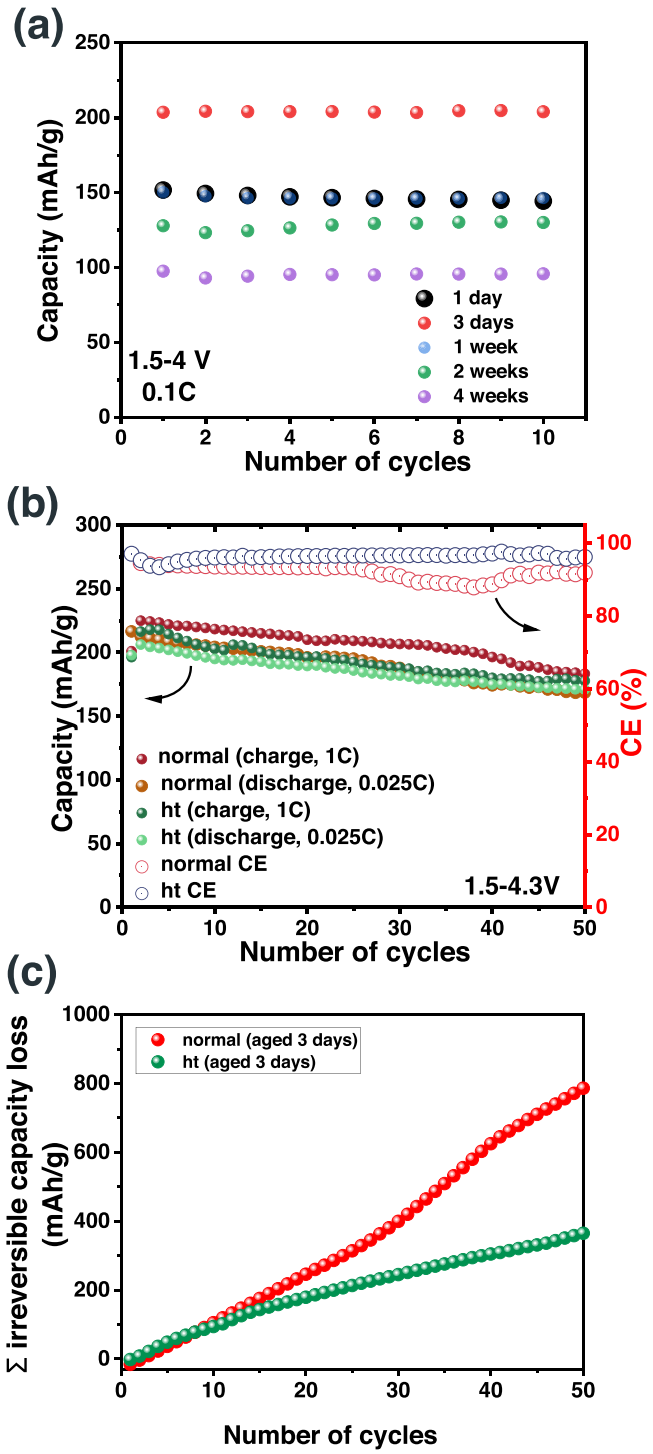

Figure 9. (a) Comparison of the capacity retention (discharge) after calendar aging of cells with LMOF33 from 1 day to 4 weeks. (b) Cyclability plots during fast charge (1 C) and slow discharge (0.025 C) regime of cells with LMOF33 without and with heat treatment and aged for 3 days, within the voltage window 1.5–4.3 V. (c) Corresponding cumulative irreversible capacity loss plot. CE Coulombic efficiency.

some amount of lithium ions could leach out from the surface of the sample.

Electrochemical results.—The galvanostatic charge and discharge data up to 100 cycles of the LMOF11 (F-poor) and LMOF33 (F-rich) samples before and after heat treatment are shown in Fig. 6. Cycling of the LMOF20 sample is also given in Fig. S6 for comparison. It is clear that although the initial capacity of the samples after heat treatment is lower (Figs. 6a, 6b), the capacity loss upon prolonged cycling seems to be much lower, and after 100 cycles the heat-treated samples presented a better stability (Figs. 6c, 6d). Based on the XPS results the lower initial capacity of the heat treated samples could be related to higher oxidation state of Mn ions. Taken together, the results show for all three compositions that the treatment was beneficial to increase the performance, specifically for the LMOF33 sample, where the capacity loss after 100 cycles was 39% before heat treatment and only 8% thereafter. Also, the cumulative irreversible capacity loss graphs shown in Figs. S7a, b indicate a significant effect of the heat treatment for LMOF11 and LMOF33, resulting in a lower capacity loss during cycling. It can be seen that the degradation process of the samples has been significantly reduced, which can be due to the change of the morphology and microstructure of the samples. In the following, the cycling of the two heat treated samples was prolonged to 200 cycles and their performance is shown in Fig. S7c. The sole effect of heat treatment is clear for both samples, however the heat treated LMOF33 sample presents a better performance, since it showed a promising discharge capacity of 165 mAh g^{-1} after 200 cycles. Consequently, this F/Li-rich cathode was selected as a model sample for further studies. The rate capability results of the heat-treated samples in the voltage window 1.5–4.3 V show a good response of all the cathodes to the change of the rate, during both charge and discharge. We have previously reported that F-poor samples can exhibit better Li^+ diffusion kinetics, however, their stability has been pointed out in comparison with F-rich composition.

Even with increased crystallite/particle size, the heat-treated samples show good kinetics, and only slight capacity decrease due to increase of the polarization at high rates (Figs. 7a, 7b). To confirm this kinetic behavior, we performed a long term cyclability test on the LMOF33 sample at different rates (Fig. 7c). Since fast charging process is a determining criterion for LIB standards, it is clear that the heat-treated samples have a stable capacity retention and good performance at both high and low rates. The observed decline of the cyclability rather at low than high rate, could be a sign of some electrolyte implications, as reported previously for the untreated materials. Figure 8 shows the electrochemical behavior of the LMOF33 sample at different voltage cut offs (4, 4.3 and 4.8 V) at the rate of 0.1 C. The charge and discharge profiles (Fig. 8a) do not show any obvious plateaus at higher voltages. The delivered discharge capacity at 4.8 V is around 300 mAh g^{-1}, however, the cells cycled at higher voltages undergo despite of higher capacities faster degradation (Fig. 8b). In order to find the most proper voltage cut off for these materials, which results in better stability, the LMOF33 sample was cycled at slow rate C/40 up to 50 cycles at different cut-off voltages between 4 and 4.4 V and all the samples were cycled from 1.5 V to the cut-off voltage. (Fig. 8c). Although it delivered the lowest initial capacity, the sample charged to 4 V showed the best capacity retention. It was found that the cells charged at higher voltages (>4.3 V) exhibited a drastic capacity fading. Accordingly, we decided to limit the voltage to 4 V and focus on the LMOF33 sample, with further surface optimization in contact with the electrolyte and at different cycling conditions.

Cells with heat treated powder were assembled and aged for different times in the Li-ion half-cells before any cycling, meaning for 1 day, 3 days, 1 week, 2 weeks and 4 weeks. This strategy allowed finding the appropriate thickness of the formed passivation layer, which is best suited to form a stable interface. Hence, we expect that surface related issues in contact with the electrolyte can be reduced. The results of these tests (depicted in Fig. 9a) led to the finding that the batteries, which have been aged for 3 days, showed the highest capacities. Hence, it turned out that the 3 days calendar aging, along with working with lower cut-off voltage, is an additional asset for long-term cycling stability of heat-treated samples. In the following, the cells made of the LMOF33 sample (before and after heat treatment) and aged for 3 days were cycled in

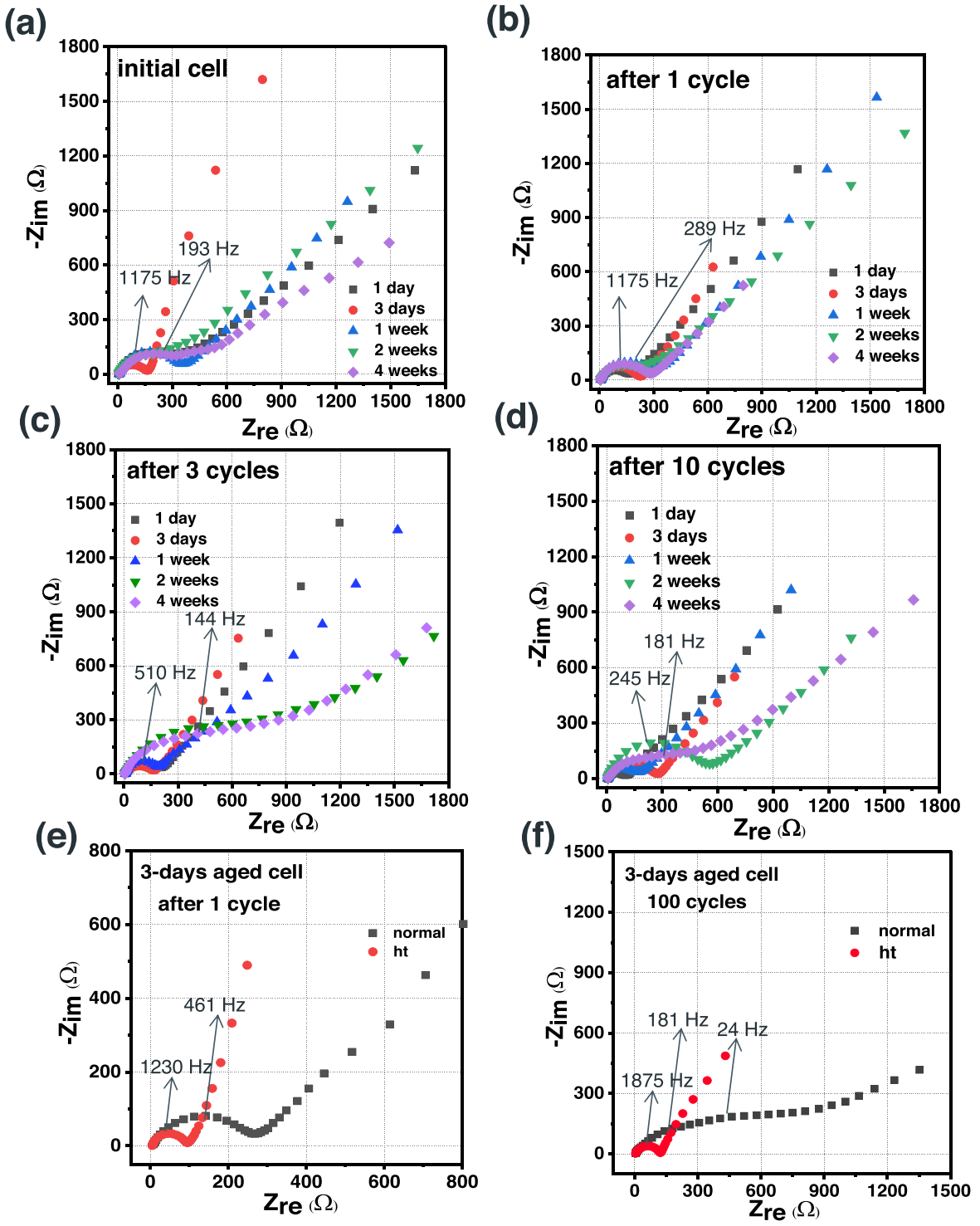

Figure 10. EIS Nyquist plots of the LMOF33 sample for (a) initial cell, (b) after 1 cycle, (c) after 3 cycles, (d) after 10 cycles, given for five aged cells by considering the time of calendar aging. Comparison of the EIS Nyquist plots of LMOF33 samples (normal and ht) with cells aged for 3 days (e) after 1st and (f) 100th cycles. In the latter case, cathode-cathode symmetric cells assembled from pre-cycled cells were used.

the voltage window 1.5–4 V. It was found that the heat treated sample showed a greatly improved stability after 200 cycles (140 mAh g^{-1}), with only 13% loss of the initial capacity at the rate of 0.1 C (Figs. S8a, b).

For many LIB applications, continuous slow discharge and full charge in a very short time (fast charge) are important.[28] In this regard, we carried out an electrochemical test for the LMOF33 sample before and after heat treatment, in which the galvanostatic charge was done at a rate of 1 C, while the discharge was performed at a different rate of 0.025 C within the same cells (Figs. 9b, 9c and S9). During the process, the discharge profile remained the same as before with no clear voltage plateaus. Here again, the sample after heat treatment showed a better performance and higher coulombic efficiencies as it is visible in Fig. 9b. More clearly, the cumulative irreversible capacity loss plots for both samples (before and after heat treatment), combined with 3 days conditioning of the cells, highlight the advantage of implementing the mild temperature sintering process, where a better cycling stability can be obtained (Fig. 9c).

In the next step, CV tests of the LMOF11, LMOF20 and LMOF33 samples were performed, before and after heat treatment (Fig. S10). The weaker oxidation and reduction peaks of the samples before heat treatment reflect changes in the active surface in comparison with heat treated samples, where the electrochemically active Mn double-redox is for example more visible in the ht-LMOF33 sample.[29] The more defined peaks of the heat-treated samples also indicate a faster electrolyte-electrode diffusion kinetics, while the non-heat treated samples exhibit a slow redox process, likely involving other side reactions. More information of CV and dQ/dV plots of the aged cells, with the same loading mass, can be found in Fig. S11, where the charge transfer becomes more important for 3-days aged cells.

EIS is a useful method for characterizing interface evolution such as aging effects. Thus, an experimental investigation of electrode calendar aging effects in Li-ion half-cells was carried out.[30] We measured the impedance of five LMOF33 cells with different calendar aging times, starting from initial fresh cells and continuing with cells after 1 day, 3 days, 1 week, 2 weeks and 4 weeks. Each time the measurements were recorded for both the initial and cycled cells in discharged state at 1.5 V, after the 1st, 3rd and 10th cycle. The results shown in Fig. 10 indicate that the cells aged for 1 day and 3 days had the lowest increase in charge transfer resistance during cycling. On the other side, the cells aged for more than 2 weeks showed faster degradation after the same cycling conditions. This trend, accompanied with lower capacity of the cells, supports the assumed degradation mechanism of the cells. The aging process is, however, complicated, in terms of reducing the active mass, crystallinity, and change of the texture and morphology of the cathode material.[31,32] Up to now, several calendar aging mechanisms are known, including the formation of by-products of the decomposition of the electrolyte at the electrode surface,[33,34] as well as dissolution of metal ions from the cathode and diffusion to the anode.[35, 36] In our case, the dissolution of Mn ions in the electrolyte, which is known for Mn-based cathode materials, could be another possible reason behind the observed degradation.[16]

In the following, we measured the impedance of the 3-days aged cells with LMOF33 (before and after heat treatment), cycled for 1 and 100 times and back in the discharged state (1.5 V) as shown in Figs. 10e, 10f. Here, symmetric cells with similar cathode materials were used to monitor surface growth in these samples. In both samples, the initial starting point and the radius of the semi-circle increased upon cycling. However, the sample after heat treatment showed a stable total resistance during cycling, and the semi-circle increased only slightly after 100 cycles; while the non-treated sample displayed a high resistance, and it turned out that a stable interface was not reached during cycling of this cell. Again, this reflects a better interface stability and lower charge transfer resistance of the sample after heat treatment, supporting the above discussion for the 3-days aged cells. The results point clearly towards a guided stabilization approach of metastable DRS materials, which was up to now a subject of debate for battery application and further development.

Conclusions

In this study, a systematic approach was followed to reach a better electrochemical stability of a disordered rocksalt $Li_{1+x}Mn_{2/3}Ti_{1/3}O_2F_x$ ($0 < x \leqslant 1$) model system. Up to now, there has been no report on a high temperature stabilization process of DRS oxyfluorides without change of the crystal structure. For that, we synthesized a series of compounds by mechanochemistry, followed by a further heat treatment process under restricted conditions. As a result, the electrochemical performance of the composite cathodes was significantly improved, mainly in terms of capacity retention and cycling stability. The initial discharge capacity of heat treated $Li_2Mn_{2/3}Ti_{1/3}O_2F$ sample was 210 mAh g^{-1}, and the capacity decreased to 165 mAh g^{-1} after 100 cycles (~80% capacity retention). Such a beneficial treatment for battery cyclability was attributed to the larger particle/crystallite size, lower specific surface area and reduced surface defects, thus, less reactivity of the cathode material with the electrolyte. Also, a remarkable surface stability and long-term cycling of the electrodes can be reached through an additional calendar aging step of the Li-ion half-cells, combined with a lower voltage cut-off (4 V), which had improved further the electrochemical performance of the cells. Our findings indicate that the cells aged for 3 days delivered higher capacity and elevated structural stability, as the cells could guarantee a capacity retention over 200 cycles, when the cut-off voltage 4 V is applied. In addition to the improved electrochemical properties, the study revealed at which extent side reactions could occur for further improvement, for instance by developing a suitable surface coating [37]. The present stabilization approach holds promise for the design of Li-rich Mn-based oxyfluoride cathode materials of battery grade with better cycling performance for next generation Li-ion batteries.

Acknowledgments

This work contributes to the research performed at CELEST (Center for Electrochemical Energy Storage Ulm-Karlsruhe). The TEM characterization experiments were performed at the Karlsruhe Nano Micro Facility (KNMF), a Helmholtz research infrastructure operated at KIT.

ORCID

A. El Kharbachi https://orcid.org/0000-0003-4332-1544

References

1. R. Chen, S. Ren, M. Knapp, D. Wang, R. Witter, M. Fichtner, and H. Hahn, *Adv. Energy Mater.*, **5**, 1401814 (2015).
2. N. Yabuuchi, M. Takeuchi, M. Nakayama, H. Shiiba, M. Ogawa, K. Nakayama, T. Ohta, D. Endo, T. Ozaki, and T. Inamasu, *Proc. Natl Acad. Sci. USA*, **112**, 7650 (2015).
3. P. Rozier and J. M. Tarascon, *J. Electrochem. Soc.*, **162**, A2490 (2015).
4. R. Chen, S. Ren, M. Yavuz, A. A. Guda, V. Shapovalov, R. Witter, M. Fichtner, and H. Hahn, *Phys. Chem. Chem. Phys.*, **17**, 17288 (2015).
5. A. Urban, J. Lee, and G. Ceder, *Adv. Energy Mater.*, **4**, 1400478 (2014).
6. J. Lee, A. Urban, X. Li, D. Su, G. Hautier, and G. Ceder, *Science*, **343**, 519 (2014).
7. M. Freire, N. V. Kosova, C. Jordy, D. Chateigner, O. Lebedev, A. Maignan, and V. Pralong, *Nat. Mater.*, **15**, 173 (2016).
8. G. Assat, C. Delacourt, D. A. Dalla Corte, and J. M. Tarascon, *J. Electrochem. Soc.*, **163**, A2965 (2016).
9. N. Yabuuchi, *Chem. Lett.*, **46**, 412 (2017).
10. C. Johnson, J. Kim, C. Lefief, N. Li, J. Vaughey, and M. Thackeray, *Electrochem. Commun.*, **6**, 1085 (2004).
11. J. Bréger, M. Jiang, N. Dupré, Y. S. Meng, Y. Shao-Horn, G. Ceder, and C. P. Grey, *J. Solid State Chem.*, **178**, 2575 (2005).
12. M. M. Thackeray, C. S. Johnson, J. T. Vaughey, N. Li, and S. A. Hackney, *J. Mater. Chem.*, **15**, 2257 (2005).
13. X. Hu, H. Guo, J. Wang, Z. Wang, X. Li, Q. Hu, and W. Peng, *Ceram. Int.*, **44**, 14370 (2018).
14. B. Jiang, B. Luo, J. Li, P. Peng, J. Chen, L. Chu, Y. Li, and M. Li, *Ceram. Int.*, **45**, 160 (2019).
15. D. Jugović, M. Mitrić, M. Milović, N. Cvjetićanin, B. Jokić, A. Umićević, and D. Uskoković, *Ceram. Int.*, **43**, 3224 (2017).
16. Y. Shirazi Moghadam, S. Dinda, A. El Kharbachi, G. Melinte, C. Kübel, and M. Fichtner, *Chem. Mater.*, **34**, 2268 (2022).
17. Y. Shirazi Moghadam, A. El Kharbachi, T. Diemant, G. Melinte, Y. Hu, and M. Fichtner, *Chem. Mater.*, **33**, 8235 (2021).
18. I. Blumenhofer, Y. Shirazi Moghadam, A. El Kharbachi, Y. Hu, K. Wang, and M. Fichtner, "Synthesis and Structure Stabilization of Disordered Rock Salt Mn/V-Based Oxyfluorides as Cathode Materials for Li-Ion Batteries." *ACS Materials Au* (2022).
19. M. Nakajima and N. Yabuuchi, *Chem. Mater.*, **29**, 6927 (2017).
20. H. Chung, Z. Lebens-Higgins, B. Sayahpour, C. Mejia, A. Grenier, G. E. Kamm, Y. Li, R. Huang, L. F. Piper, and K. W. Chapman, *J. Mater. Chem. A*, **9**, 1720 (2021).
21. H. Lee, W. Choi, W. Lee, J. H. Shim, Y. M. Kim, and W. S. Yoon, *Adv. Energy Mater.*, **11**, 2002958 (2021).
22. R. Dominko, C. V.-A. Garrido, M. Bele, M. Kuezma, I. Arcon, and M. Gaberscek, *J. Power Sources*, **196**, 6856 (2011).
23. H. Ji, D. A. Kitchaev, Z. Lun, H. Kim, E. Foley, D.-H. Kwon, Y. Tian, M. Balasubramanian, M. Bianchini, and Z. Cai, *Chem. Mater.*, **31**, 2431 (2019).
24. J. Chable, C. Baur, J. H. Chang, S. Wenzel, J. M. García-Lastra, and T. Vegge, *J. Phys. Chem.*, C **124**, 2229 (2019).
25. J. Mayer, U. Diebold, T. Madey, and E. Garfunkel, *J. Electron. Spectrosc. Relat. Phenom.*, **73**, 1 (1995).

26. M. Oku, K. Hirokawa, and S. Ikeda, *J. Electron. Spectrosc. Relat. Phenom.*, **7**, 465 (1975).
27. J. H. Lee, Y. J. Sa, T. K. Kim, H. R. Moon, and S. H. Joo, *J. Mater. Chem. A*, **2**, 10435 (2014).
28. L. Xu and B. Lu, *Electrochim. Acta*, **210**, 456 (2016).
29. Y. Zhang, P. Hou, E. Zhou, X. Shi, X. Wang, D. Song, J. Guo, and L. Zhang, *J. Power Sources*, **292**, 58 (2015).
30. U. Tröltzsch, O. Kanoun, and H.-R. Tränkler, *Electrochim. Acta*, **51**, 1664 (2006).
31. J. P. Pender, G. Jha, D. H. Youn, J. M. Ziegler, I. Andoni, E. J. Choi, A. Heller, B. S. Dunn, P. S. Weiss, and R. M. Penner, *ACS nano*, **14**, 1243 (2020).
32. V. Agubra and J. Fergus, *Materials*, **6**, 1310 (2013).
33. M. Wohlfahrt-Mehrens, C. Vogler, and J. Garche, *J. Power Sources*, **127**, 58 (2004).
34. T. Waldmann, M. Wilka, M. Kasper, M. Fleischhammer, and M. Wohlfahrt-Mehrens, *J. Power Sources*, **262**, 129 (2014).
35. M. Klett, R. Eriksson, J. Groot, P. Svens, K. C. Högström, R. W. Lindström, H. Berg, T. Gustafson, G. Lindbergh, and K. Edström, *J. Power Sources*, **257**, 126 (2014).
36. M. Dubarry, C. Truchot, B. Y. Liaw, K. Gering, S. Sazhin, D. Jamison, and C. Michelbacher, *J. Power Sources*, **196**, 10336 (2011).
37. Y. Shirazi Moghadam, A. El Kharbachi, M. A. Cambaz, S. Dinda, T. Diemant, Y. Hu, G. Melinte, and M. Fichtner, "Borate-Based Surface Coating of Li-Rich Mn-Based Disordered Rocksalt Cathode Materials." *Adv. Mater. Interfaces*, **9**, 2201200 (2022).